A&A 474, 609–615 (2007)
DOI: 10.1051/0004-6361:20077648

Astronomy & Astrophysics

Coronal ion-cyclotron beam instabilities within the multi-fluid description

R. Mecheri and E. Marsch

Max-Planck Institut für Sonnensystemforschung, Max-Planck Strasse 2, 37191 Katlenburg-Lindau, Germany
e-mail: mecheri@mps.mpg.de

Received 15 April 2007 / Accepted 26 June 2007

ABSTRACT

Context. Spectroscopic observations and theoretical models suggest resonant wave-particle interactions, involving high-frequency ion-cyclotron waves, as the principal mechanism for heating and accelerating ions in the open coronal holes. However, the mechanism responsible for the generation of the ion-cyclotron waves remains unclear. One possible scenario is that ion beams originating from small-scale reconnection events can drive micro-instabilities that constitute a possible source for the excitation of ion-cyclotron waves.
Aims. We use the multi-fluid model in the low-β coronal plasma to study ion beam-driven electromagnetic instabilities. By neglecting the electron inertia this model allows one to take into account ion-cyclotron wave effects that are absent from the one-fluid magneto-hydrodynamics (MHD) model. Realistic models of density and temperature as well as a 2-D analytical magnetic field model are used to define the background plasma in the open-field funnel region of a polar coronal hole.
Methods. Taking into account the WKB (Wentzel-Kramers-Brillouin) approximation, a Fourier plane-wave linear mode analysis is employed to derive the dispersion relation. The ray-tracing theory is used to compute the ray path of the unstable wave as well as the evolution of the growth rate of the wave while propagating in the coronal funnel.
Results. We demonstrate that in typical coronal hole conditions and assuming realistic values of the beam velocity, the free energy provided by the ion beam propagating parallel to the ambient field can drive micro-instabilities through resonant ion-cyclotron excitation.

Key words. Sun: corona – waves – instabilities

1. Introduction

Observations made by the Ultraviolet Coronagraph Spectrometer (UVCS) and other instruments at the Solar and Heliospheric Observatory (SOHO) have significantly increased our knowledge of the kinetic properties of charged particles close to the Sun in the source region of the fast solar wind. Spectroscopic determination of the widths of ultraviolet emission lines in coronal holes indicate that heavy ions are very hot and have high temperature anisotropies, and that heavier ions have a higher temperature than the protons by at least their mass ratio, i.e. $T_i/T_p > m_i/m_p$ (Kohl et al. 1997; Cranmer et al. 1999). These observations strongly suggest that resonant ion-cyclotron wave-particle interaction is a major mechanism for the heating and acceleration of ions in the magnetically open corona. This notion led to renewed interest in models involving ion heating by high-frequency ion-cyclotron waves (Isenberg et al. 2000; Hollweg 2000; Marsch & Tu 2001; Vocks & Marsch 2001; Xie et al. 2004). For a detailed review on resonant ion-cyclotron interactions in the corona, see Hollweg & Isenberg (2002).

However, it remains unclear how these waves originate in the solar corona, and whether they are generated locally or emanate from the coronal base. One possible scenario is that the ion-cyclotron waves are generated in the lower corona by small-scale reconnection events as suggested by Axford & McKenzie (1992). They might also be generated locally through a turbulent cascade of low-frequency MHD-type waves towards high-frequency ion-cyclotron waves (Li et al. 1999; Hollweg 2000; Ofman et al. 2002), or by plasma micro-instabilities driven by current fluctuations of low-frequency MHD modes (Markovskii 2001), or by an intermittent electron heat flux accompanying microflare events (Markovskii & Hollweg 2004). Voitenko & Goossens (2002) further suggested that plasma outflows from reconnection sites in microflares could create ion-beam configurations in the surrounding plasma, and thus provide free energy for driving kinetic micro-instabilities through ion-cyclotron resonance and the Cerenkov effect. The possible origin of the ion beams observed in the solar wind from reconnection jets and explosive events in the corona was proposed by Feldman et al. (1996).

Indeed, detailed spectroscopic studies of the so-called high-velocity events and explosive events using spectra obtained with the Coronal Diagnostic Spectrometer (CDS; Brekke et al. 1997) and the Solar Ultraviolet Measurement of Emitted Radiation instrument (SUMER; Innes et al. 1997) both at the SOHO, revealed a new character of the lower corona as a highly dynamic medium. They signify the omni-presence of transient explosive events and a wide variety of plasma jets with velocities ranging from a few tens of a kilometer per second up to several hundreds of kilometers per second. Since these plasma jets have been observed to evolve in a similar way as that predicted by the theory of magnetic reconnection (Innes et al. 1997), explosive events and plasma jets have been associated with the highly-dynamic small-scale reconnections which are supposed

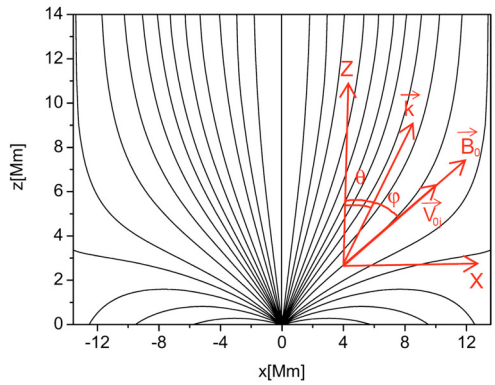

Fig. 1. Magnetic field geometry of a funnel as obtained from the 2-D potential-field model derived by Hackenberg et al. (2000). The field lines emerge from the boundary between two adjacent supergranules ($x = 0$) and expand rapidly to fill the corona. The photospheric level is at $z = 0$. Coordinate axes, wave vector and beam drift velocity are shown in red.

to take place in the chromospheric network, approximately at heights of 1000−3000 km above the photosphere. Solar magnetograms provided by the Michelson Doppler Imager (MDI) at the SOHO clearly indicate that the magnetic network field exists in two characteristic components, i.e. in a few unipolar open flux tubes, "funnels", and in multiple closed flux tubes, "loops", (Schrijver et al. 1998). The magnetic network is very dynamic and releases non-potential-field magnetic energy which is converted into plasma heating, beam particles, and motion of the coronal plasma. All these processes provide ample free energy for driving plasma macro- and micro-instabilities.

The present paper aims to study the possible occurrence of these instabilities in typical conditions for coronal holes. We focus particularly on beam-driven instabilities in the ion-cyclotron frequency range which are driven by the presence of tenuous ion beams, presumably originating from small-scale reconnection sites and propagating parallel to the ambient magnetic field. Linear mode analysis is used in the framework of the multi-fluid model, while neglecting the electron inertia. This model permits the consideration of ion-cyclotron-wave effects that are absent from the one-fluid MHD model. Realistic models of the density and temperature, as well as a 2-D funnel model describing the open-field region, are used to define the background plasma. Considering the WKB approximation (in which the wavelength of interest is assumed to be smaller than the non-uniformity length scale), we first solve the dispersion relation locally and then perform a non-local wave analysis using the ray-tracing theory, which allows us to compute the ray paths of the unstable waves in the funnel as well as the spatial variation of their growth rates.

This paper is structured as follows. In Sect. 2, we present the 2-D analytical funnel model used in this study to describe open-field region in a coronal hole. Then in Sect. 3, we describe how the local and non-local (ray-tracing) linear perturbation analysis using the multi-fluid model is carried out. The results are presented and discussed in Sect. 4, and finally we give our conclusions in Sect. 5.

2. Background plasma configuration

For the background plasma density and temperature we use the model parameters of Fontenla et al. (1993) for the chromosphere and Gabriel (1976) for the lower corona. The 2-D potential-field model derived by Hackenberg et al. (2000) is used to define the background magnetic field (Fig. 1) in the funnel. Analytically, the two components of this model field are given by:

$$B_{0x}(x,z) = \frac{(B_{\max}-B_{00})L}{2\pi(L-d)} \ln \frac{\cosh\frac{2\pi z}{L} - \cos\left(\frac{\pi d}{L}+\frac{2\pi x}{L}\right)}{\cosh\frac{2\pi z}{L} - \cos\left(\frac{\pi d}{L}-\frac{2\pi x}{L}\right)} \tag{1}$$

$$\begin{aligned} B_{0z}(x,z) \;=\; & B_{00} + (B_{\max}-B_{00})\left[-\frac{d}{L-d}+\frac{L}{(L-d)\pi}\right. \\ & \times\left(\arctan\frac{\cosh\frac{2\pi z}{L}\,\sin\frac{\pi d}{2L}+\sin\left(\frac{\pi d}{2L}+\frac{2\pi x}{L}\right)}{\sinh\frac{2\pi z}{L}\,\cos\frac{\pi d}{2L}}\right. \\ & \left.\left.+\arctan\frac{\cosh\frac{2\pi z}{L}\,\sin\frac{\pi d}{2L}+\sin\left(\frac{\pi d}{2L}-\frac{2\pi x}{L}\right)}{\sinh\frac{2\pi z}{L}\,\cos\frac{\pi d}{2L}}\right)\right]. \end{aligned} \tag{2}$$

The typical parameters relevant for this model are: $L = 30$ Mm, $d = 0.34$ Mm, $B_{00} = 11.8$ G, and $B_{\max} = 1.5$ kG.

3. Linear perturbation analysis

To describe wave propagation in the funnel we use the multi-fluid equations and subject them to a linear perturbation analysis. The fluid equations associated with the polytropic gas law for any particle species j are given by:

$$\frac{\partial n_j}{\partial t} + \nabla\cdot(n_j \boldsymbol{v}_j) = 0, \tag{3}$$

$$\begin{aligned} & m_j n_j\left(\frac{\partial \boldsymbol{v}_j}{\partial t} + \boldsymbol{v}_j\cdot\nabla\boldsymbol{v}_j\right) + \nabla p_j - q_j n_j(\boldsymbol{E}+\boldsymbol{v}_j\times\boldsymbol{B}) \\ & + m_j n_j \sum_{j'} \nu_{jj'}(\boldsymbol{v}_j - \boldsymbol{v}_{j'}) = 0, \end{aligned} \tag{4}$$

$$p_j n_j^{-\gamma_j} = \text{const.}, \tag{5}$$

where m_j, n_j, $\boldsymbol{v}_j$, p_j and γ_j(=5/3) are respectively the mass, density, velocity, pressure and the adiabatic polytropic index of a species j. Subscript j stands for electron e, proton p or alpha particle α (He^{2+}). The quantity $\nu_{jj'}$ is the collision frequency of a particle of species j with particles of species j' (only the electron-proton collisions are taken into account). The electric field $\boldsymbol{E}$ and the magnetic field $\boldsymbol{B}$ are linked by Faraday's law:

$$\nabla\times\boldsymbol{E} = -\frac{\partial \boldsymbol{B}}{\partial t}. \tag{6}$$

3.1. Linearization procedure

The linear perturbation analysis is performed by expressing all the quantities in the fluid equations as a sum of an unperturbed stationary part (with subscript 0) and a perturbed part (with subscript 1) that is much smaller than the stationary part:

$$n_j = n_{0j}(z) + n_{1j},\; T_j = T_{0j}(z) + T_{1j},\; p_j = p_{0j}(z) + p_{1j},$$

$$\boldsymbol{v}_j = \boldsymbol{v}_{0j} + \boldsymbol{v}_{1j},\; \boldsymbol{B} = \boldsymbol{B}_0(x,z) + \boldsymbol{B}_1,\; \boldsymbol{E} = \boldsymbol{E}_0 + \boldsymbol{E}_1,$$

$$\text{with}: \; n_{1j} \ll n_{0j},\;\; T_{1j} \ll T_{0j},\;\; p_{1j} \ll p_{0j},\;\; |\boldsymbol{v}_{1j}| \ll |\boldsymbol{v}_{0j}|,$$

$$|\boldsymbol{B}_1| \ll |\boldsymbol{B}_0|,\;\; |\boldsymbol{E}_1| \ll |\boldsymbol{E}_0| \quad\text{and}\quad \boldsymbol{v}_{0j}\times\boldsymbol{B}_0 = 0. \tag{7}$$

We assume charge neutrality and a current-free state for the unperturbed stationary plasma, i.e., $\sum_j q_j n_{0j} = 0$ and

$\sum_j q_j n_{0j} \boldsymbol{v}_{0j} = 0$. The zero-order terms cancel out when Eq. (7) is inserted into the multi-fluid Eqs. (3)−(5). Neglecting the nonlinear products of the first-order terms, we get a system of coupled linear equations:

$$\mathrm{i}(\omega - \boldsymbol{k}\cdot\boldsymbol{v}_{0j})\frac{n_{1j}}{n_{0j}} - \mathrm{i}\boldsymbol{k}\cdot\boldsymbol{v}_{1j} = 0, \tag{8}$$

$$\mathrm{i}(\omega - \boldsymbol{k}\cdot\boldsymbol{v}_{0j})\boldsymbol{v}_{1j} + \Omega_j\left(\frac{\boldsymbol{E}_1}{|\boldsymbol{B}_0|} + \boldsymbol{v}_{1j}\times\frac{\boldsymbol{B}_0}{|\boldsymbol{B}_0|} + \boldsymbol{v}_{0j}\times\frac{\boldsymbol{B}_1}{|\boldsymbol{B}_0|}\right)$$
$$-\mathrm{i}C_{sj}^2\frac{p_{1j}}{p_{0j}}\boldsymbol{k} - \sum_{j'}\nu_{jj'}(\boldsymbol{v}_{1j} - \boldsymbol{v}_{1j'}) = 0, \tag{9}$$

$$\frac{p_{1j}}{p_{0j}} - \gamma_j\frac{n_{1j}}{n_{0j}} = 0, \tag{10}$$

$$\mathrm{i}\boldsymbol{k}\times\boldsymbol{E}_1 = \mathrm{i}\omega\boldsymbol{B}_1, \tag{11}$$

where all the perturbed quantities have been expressed in the form of a plane wave. This Fourier analysis turns all derivatives into algebraic factors, i.e. $\partial/\partial t \rightarrow -\mathrm{i}\omega$ and $\nabla \rightarrow \mathrm{i}\boldsymbol{k}$, where ω is the wave frequency and $\boldsymbol{k}$ the wave vector. In the above equations, $C_{sj} = \sqrt{\gamma_j k_\mathrm{B} T_j/m_j}$ is the acoustic speed and $\Omega_j = eB_0/m_j$ the cyclotron frequency of species j, and k_B is the Boltzman constant.

3.2. Dispersion relation

To derive the dispersion relation, the above linearized equations have to be combined in order to obtain a linear relation between the current density $\boldsymbol{J}_1$ and the electric field $\boldsymbol{E}_1$:

$$\boldsymbol{J}_1 = \boldsymbol{\sigma}\cdot\boldsymbol{E}_1, \tag{12}$$

where $\boldsymbol{\sigma}$ is the conductivity tensor which is related to the dielectric tensor $\boldsymbol{\epsilon}$ through the following relation:

$$\boldsymbol{\epsilon}(\omega,\boldsymbol{k},\boldsymbol{r}) = \boldsymbol{I} + \frac{\mathrm{i}}{\omega\varepsilon_0}\boldsymbol{\sigma}(\omega,\boldsymbol{k},\boldsymbol{r}). \tag{13}$$

Finally, the local dispersion relation is obtained using the theory of electrodynamics (e.g., Stix 1992):

$$D(\omega,\boldsymbol{k},\boldsymbol{r}) = \mathrm{Det}\left[\frac{c^2}{\omega^2}\boldsymbol{k}\times(\boldsymbol{k}\times\boldsymbol{E}) + \boldsymbol{\epsilon}(\omega,\boldsymbol{k},\boldsymbol{r})\cdot\boldsymbol{E}\right] = 0, \tag{14}$$

where c is the speed of light in vacuum and $\boldsymbol{r}$ is the large-scale position vector. We choose the wave vector $\boldsymbol{k}$ to lie in the $x-z$ plane, with $\boldsymbol{k} = k(\sin\theta, 0, \cos\theta)$.

3.3. Ray-tracing equations

In the framework of the WKB approximation, the-ray tracing problem consists at solving a system of ordinary differential equations of the Hamiltonian form (Weinberg 1962). The ray-tracing equations, which represent the equations of motion for the wave frequency ω, the wave vector $\boldsymbol{k}$, and the space coordinate $\boldsymbol{r}$, have been formulated by Bernstein & Friedland (1984). In the simple case of a Hermitian dielectric tensor, they are given by:

$$\frac{\mathrm{d}\omega}{\mathrm{d}t} = -\frac{\partial D(\omega,\boldsymbol{k},\boldsymbol{r})/\partial t}{\partial D(\omega,\boldsymbol{k},\boldsymbol{r})/\partial\omega} = 0, \tag{15}$$

$$\frac{\mathrm{d}\boldsymbol{k}}{\mathrm{d}t} = \frac{\partial D(\omega,\boldsymbol{k},\boldsymbol{r})/\partial\boldsymbol{r}}{\partial D(\omega,\boldsymbol{k},\boldsymbol{r})/\partial\omega}, \tag{16}$$

$$\frac{\mathrm{d}\boldsymbol{r}}{\mathrm{d}t} = -\frac{\partial D(\omega,\boldsymbol{k},\boldsymbol{r})/\partial\boldsymbol{k}}{\partial D(\omega,\boldsymbol{k},\boldsymbol{r})/\partial\omega}. \tag{17}$$

A generalization of these equations to the case of an anti-Hermitian dielectric tensor was also proposed by Bernstein & Friedland (1984). In this case, in addition to the ray path, the growth rate of the instability can be computed. Note that Eq. (15) can be set to zero, because the dispersion relation does not explicitly depend on the time t (the background plasma is stationary). The above set of differential equations represents an initial-value problem which can be solved by using the initial conditions obtained from the local solutions of the dispersion relation (Eq. (14)).

4. Numerical results

We assume that the ion-beam particles are generated at the funnel location at $x = 7.5$ Mm and $z = 2.2$ Mm, presumably by small scales reconnection events. This location is characterized by a magnetic field inclination angle of $\varphi = 82°$ with respect to the normal on the solar surface. According to the observations, the calculations will be performed for a beam velocity equal to 320 km s^{-1}. We consider the case of an alpha particle (He^{2+}) beam plasma configuration, propagating parallel to the ambient field. For comparison purposes, the dispersion diagrams in the case of a plasma without the beam are also presented. We first present the results obtained from the local solutions of the dispersion relation, Eq. (14) and then the results obtained from the non-local wave analysis using the ray-tracing equations.

4.1. Local stability analysis

4.1.1. Zero beam plasma

For $v_{0\alpha} = 0$ and $\theta = 30°$, the dispersion diagram in the case of the two-fluid (e-p) model (left panels of Fig. 2) shows the presence of three stable modes, each one of them is represented by an oppositely propagating ($\omega > 0$ and $\omega < 0$) pair of waves. These modes represent the extensions of the usual Slow (red line), Alfvén (green line) and Fast (blue line) MHD modes into the high-frequency domain around $\omega = \Omega_\mathrm{p}$ ($=eB_0/m_\mathrm{p}$), where the waves are dispersive (for details see Mecheri & Marsch 2006). In the case of the three fluid (e-p-He^{2+}) model (right panels of Fig. 2) five stable modes are present (each one represented by an oppositely propagating pair of waves). These modes are: two slow modes (yellow and red lines), two ion-cyclotron modes (gray and green lines) and one fast mode (blue line). The waves are subject to mode conversion or coupling, a phenomenon associated with the appearance of a cut-off frequency concerning the fast mode (for details see Mecheri & Marsch 2006).

4.1.2. Alpha particles beam

The alpha particle beam configuration consists of three species: electrons (with density $n_{0\mathrm{e}}$), protons (with density $n_{0\mathrm{p}}$) and a tenuous beam of alpha particles, He^{2+} indicated by α, with a velocity $v_{0\alpha}$ parallel to the ambient magnetic field $\boldsymbol{B}_0$ and a density $n_{0\alpha} = 0.1 n_{0\mathrm{p}}$. The protons are considered to be at rest and the electrons are in motion with a velocity $v_{0\mathrm{e}}$. Alphas and electrons satisfy thus the zero-current condition, $v_{0\mathrm{e}} = 2(n_{0\alpha}/n_{0\mathrm{e}})v_{0\alpha}$. The alpha particle beam relative density is taken from in-situ observations made by the Helios spacecraft, with $n_{0\alpha}/n_{0\mathrm{e}} \approx n_{0\alpha}/n_{0\mathrm{p}} = 0.05-0.2$ (Tu et al. 2004). This choice is justified since it has been argued by Feldman et al. (1996) that the alpha beams might

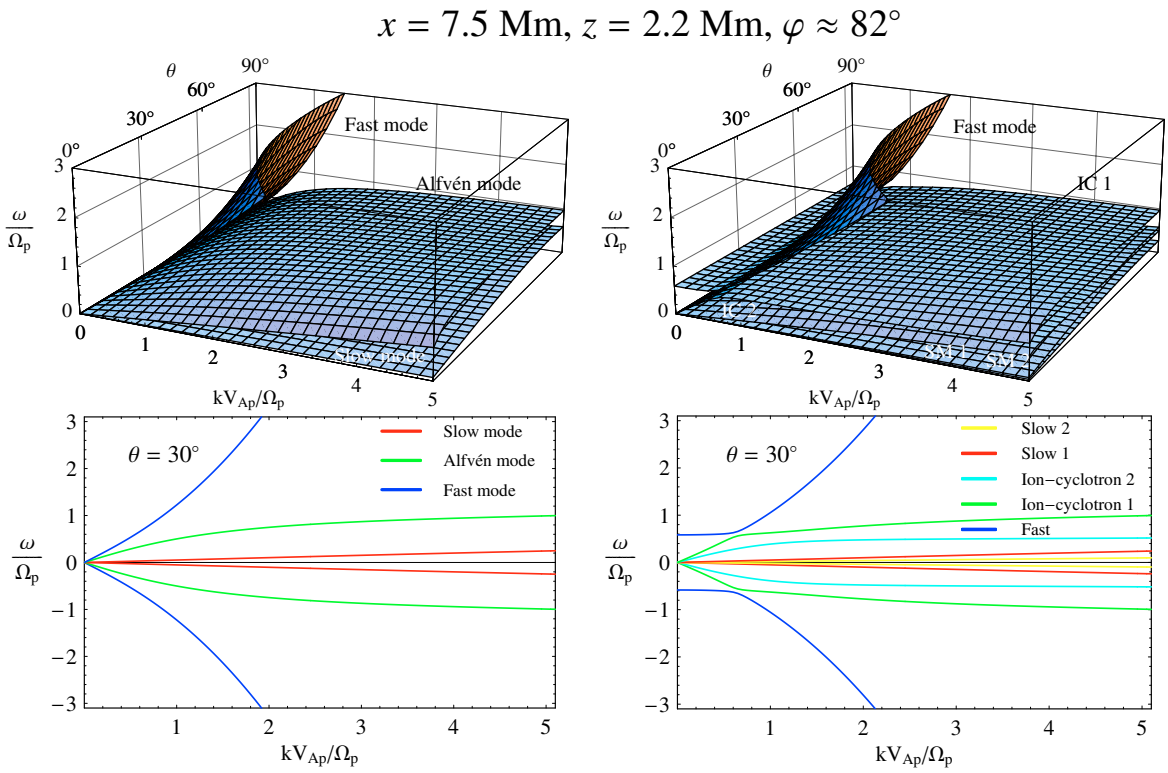

Fig. 2. Two-fluid (e-p plasma on the left panels) and three-fluid (e-p-He^{2+} plasma on the right panels) dispersion surfaces (*top panels*) and single curves (for $\theta = 30°$ at the bottom) for the case of a zero beam speed, i.e. $v_{0\alpha} = 0$. The alpha particle (He^{2+}) density is $n_{0\alpha} = 0.1n_{0p}$ and the plasma beta values are $\beta_e = 0.0043 = 1.2\beta_p = 12\beta_\alpha$. Here ω and k are normalized, respectively, to the proton cyclotron frequency, Ω_p, and the inertial length, Ω_p/V_{Ap}, where $V_{Ap} = B_0/\sqrt{\mu_0 n_{0p} m_p}$ is the proton Alfvén speed (μ_0 is the magnetic permeability in the vacuum). Here $T_{0e} = T_{0p} = T_{0\alpha} = 1.35 \times 10^4$ K, $n_{0p} = 3.73 \times 10^{16}$ m^{-3}, $B_0 = 15.54$ Gauss.

originate from reconnection events at the base of the expanding solar corona. In this case (i.e. $v_{0b} \neq 0$), the dispersion curves are strongly modified by the appearance of regions of instability associated with two cyclotron beam modes (Fig. 3), which in the cold-plasma case are characterized by the dispersion relations (Cap 1978):

$$\omega_b \approx \begin{cases} kv_{0\alpha}\, cos(\varphi - \theta) + \Omega_\alpha & \text{cyclotron beam 1} \\ kv_{0\alpha}\, cos(\varphi - \theta) - \Omega_\alpha & \text{cyclotron beam 2.} \end{cases} \quad (18)$$

It should be noted that the values of the electron-proton collision frequency in this region of the solar atmosphere (i.e. $\nu_{ep}/\Omega_p \approx 11.6$ and $\nu_{pe}/\Omega_p \approx 0.006$) are large enough to make the perturbed electron and proton velocities equal, but the alpha differential motion (which provides the free energy) remains unaffected, because the initial beam velocity considered is rather high, and the collisional slowing-down time declines exponentially with the drift in units of the ion thermal speed (e.g., Boyd & Sanderson 1969).

For $\theta = 15°$ (top panel), the instability results from the intersection between the ion-cyclotron mode (ω_L) and the cyclotron beam mode 2. This region of instability is indicated by (L) in reference to the left-hand polarization characterizing the ion-cyclotron mode. Indeed, these two distinct and initially stable modes merge, within a certain range (corresponding to the red curve) of the wave number k, into one single unstable mode which satisfies the resonance condition:

$$\omega \approx kv_{0\alpha}\ cos(\varphi - \theta) - \Omega_\alpha. \quad (19)$$

This condition corresponds to a left-hand resonant cyclotron excitation of the ion-cyclotron mode through the anomalous Doppler effect (Gary 1993). As shown in the left panel of Fig. 4, this instability extends from smaller k, at propagation angles around $\theta \approx 60°$ with a small growth rate, i.e. $\gamma \approx 0.03\Omega_p$, to higher k and to smaller angles of propagation with a larger growth rate, i.e. $\gamma \approx 0.12\Omega_p$. Since the location at $x = 7.5$ Mm and $z = 2.2$ Mm is characterized by a $\boldsymbol{B}_0$-inclination angle $\varphi = 82°$, we can therefore say that as k increases this instability tends to appear at increasingly oblique propagation angles with respect to the ambient magnetic field, and its growth rate tends to maximize for perpendicular propagation. In the middle panel of Fig. 4 the left-hand resonant instability is shown as a function of θ and $n_{0\alpha}$, for the case of $v_{0\alpha} = 320$ km s^{-1} $\approx 1.8V_{Ap}$ and a normalized wave number $kV_{Ap}/\Omega_p = 0.5$. It is clearly seen that the growth rate of the instability increases with increasing $n_{0\alpha}$ and gradually is also covering a wider range of θ, but it stays below approximately $\theta \approx 60°$. The maximum growth rate is $\gamma \approx 0.1\Omega_p$ for $n_{0\alpha} = 0.2n_{0p}$ and $\theta \approx 25°$. This instability is also presented on the right panel of Fig. 4 as a function of θ and $v_{0\alpha}$ and for $n_{0\alpha}/n_{0p} = 0.1$ and $kV_{Ap}/\Omega_p = 0.5$. It is clearly seen that the instability has a threshold in the beam velocity $v_{0\alpha}$ below which it does not occur. This threshold depends on θ and increases from $v_{0\alpha} \approx 1.5V_{Ap}$ at $\theta \approx 60°$ to $v_{0\alpha} \approx 2V_{Ap}$ for quasi-perpendicular propagation $\theta \approx 0°$ (knowing that the inclination angle of $\boldsymbol{B}_0$ is $\varphi \approx 82°$).

On the other hand, for $v_{0\alpha} \neq 0$ and an angle of propagation $\theta = 65°$ (bottom of Fig. 3), the results show the disappearance of the left-hand resonant instability involving the ion-cyclotron mode and the appearance of another kind of instability involving the right-handed polarized fast mode, from which the name right-hand resonant instability is derived. This instability is indicated by (R) and results from the intersection of the

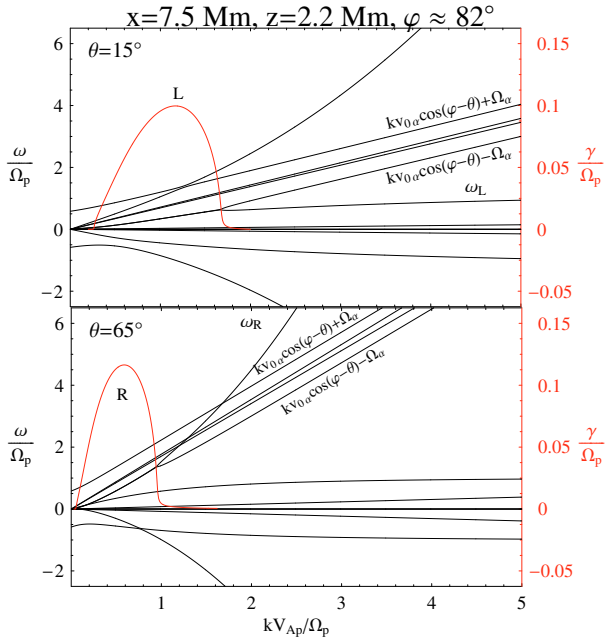

Fig. 3. Wave frequency (black) and growth rate (red) in an alpha particle beam plasma ($n_{0\alpha}/n_{0p} = 0.1$ and $v_{0\alpha} = 320\ \mathrm{km\,s^{-1}} \approx 1.8V_{Ap}$) versus wave vector for two propagation angles θ. Note, that for $\theta = 15°$ (i.e., quasi-perpendicular propagation, *top panel*), the left-hand resonant ion-cyclotron mode (ω_L) is excited, and that for $\theta = 65°$ (i.e., quasi-parallel propagation, *bottom panel*) the right-hand resonant fast mode (ω_R) is excited, whereby both satisfy the condition Eq. (19) for the anomalous Doppler effect. Here $T_{0e} = T_{0p} = T_{0\alpha}$.

fast mode (ω_R) with the cyclotron beam mode 2 satisfying the resonance condition Eq. (19). As shown on the left panel of Fig. 5 this instability is mainly centered around a normalized wave number $kV_{Ap}/\Omega_p \approx 0.5$, and has maximum growth rate $\gamma \approx 0.13\Omega_p$ at a large angle of propagation $\theta \approx 90°$. The right-hand resonant instability vanishes for highly oblique propagation with respect to the ambient field (knowing that the inclination of $\boldsymbol{B}_0$ in this location is $\varphi \approx 82°$), and the wave amplitude grows strongly for decreasing obliquity of the propagation angle. In the middle panel of Fig. 5, the right-hand resonant instability is shown as a function of θ and $n_{0\alpha}$, for the case of $v_{0\alpha} = 320\ \mathrm{km\,s^{-1}} \approx 1.8V_{Ap}$ and $kV_{Ap}/\Omega_p = 0.5$. It is clearly seen that the growth rate of this instability increases with increasing $n_{0\alpha}$. This behavior is more pronounced for higher θ, which corresponds to decreasingly oblique propagation. The maximum growth rate, $\gamma \approx 0.16\Omega_p$, is obtained for $n_{0\alpha} = 0.2n_{0p}$ and $\theta \approx 80°$. We can also see that the instability fades away for small propagation angles, with $\theta \lesssim 40°$, which corresponds to quasi-perpendicular propagation (with respect to the field). In the same figure (on the right panel) we also present the dependence of this instability upon θ and $v_{0\alpha}$ for $n_{0\alpha}/n_{0p} = 0.1$ and $kV_{Ap}/\Omega_p = 0.5$. It can be seen, similar to the left-hand instability, that this instability has a threshold in the beam velocity $v_{0\alpha}$, below which it does not occur. This threshold depends on θ and increases from $v_{0\alpha} \approx 1.6V_{Ap}$ at large angle of propagation, $\theta \approx 90°$ (quasi-parallel propagation since $\varphi = 82°$), to $v_{0\alpha} \approx 2.5V_{Ap}$ at $\theta \approx 25°$ (quasi-perpendicular propagation).

4.2. Non-local stability analysis

In this section we go beyond the local treatment of the waves and perform a non-local wave study using the ray-tracing equations. The ray-tracing equations are solved employing the initial conditions obtained from the local solutions of the dispersion relation Eq. (14) at the location with $x_0 = 7.5$ Mm and $z_0 = 2.2$ Mm. We consider the case of an alpha particle (He^{2+}) beam plasma configuration with a constant concentration, $n_\alpha = 0.1n_p$, and a constant beam velocity of $v_{0\alpha} = 320\ \mathrm{km\,s^{-1}}$.

The ray paths of the unstable waves as well as the variation of their growth rates as a function of height z, when the wave is launched at the initial location ($x_0 = 7.5$ Mm and $z_0 = 2.2$ Mm) which is characterized by a strong inclination angle ($\varphi \approx 82°$) of the magnetic field with respect to the normal on the solar surface, are illustrated in Fig. 6. The results are presented for a different initial angle of propagation, θ_0, with which an initial wave number k_0 (normalized to Ω_p/V_{Ap}) is associated and chosen so as to correspond to the maximum growth rate, γ_{max}.

Our results show that the ray path of the left-hand unstable wave (Fig. 6, on the left) is strongly affected by the closed-field geometry characterizing this funnel region. Indeed, this unstable wave starting from its initial position propagates upward in the coronal funnel to a certain height, where it turns down again and starts propagating downward to return back to the initial height. The associated instability growth rate decreases along that ray path. Since the direction of the group velocity is always parallel to the ray path and indicates where the energy is transported, we can say that the energy associated with the left-hand resonant instability does not reach high altitudes in the funnel. The smaller θ_0 is, the higher up this unstable wave propagates in the funnel.

The right-hand unstable wave (Fig. 6, on the right) is also found to be well guided and, depending on θ_0, can follow both closed and open coronal field lines, which may exist side by side in this region of the funnel. Indeed, for $\theta_0 = 50°$ and $\theta_0 = 55°$ the unstable wave propagates along the open magnetic field lines and reaches high altitudes in the funnel up to 15 Mm, while for $\theta_0 = 60°$, $65°$ and $70°$, similar to the left-hand instability, the right-hand resonant unstable waves are affected by the closed-field geometry and reflected back towards lower altitudes in the funnel. Thus, the energy associated with this instability is also transported along the magnetic field lines, but eventually to much greater altitude (i.e. $z = 15$ Mm) in the funnel, as compared to the left-hand instabilities. For $\theta_0 = 50°$ and $\theta_0 = 55°$ the growth rate of the right-hand instability first increases until altitudes of $z \approx 3.25$ Mm and $z \approx 3.75$ Mm respectively, where it starts to sharply decrease and cancels at $z \approx 3.6$ Mm and $z \approx 4.5$ Mm respectively. On the other hand, for $\theta_0 = 60°$, $65°$ and $70°$, the growth is first slightly increased during the upward propagation phase, and then it rapidly decreases to zero while the wave is propagating downward.

5. Conclusion

We have studied beam-driven electromagnetic instabilities near the ion-cyclotron frequency in a coronal funnel using the multi-fluid model. We have considered the case of an alpha particle beam propagating in the funnel parallel to the ambient magnetic field lines. In agreement with kinetic dispersion theory, the local solutions of the dispersion relation revealed the presence of two kinds of instabilities: the left-hand and right-hand resonant instabilities. The left-hand and right-hand instabilities arise from the resonant excitation of the left-hand-polarized ion-cyclotron mode and right-hand-polarized fast mode respectively through the anomalous Doppler effect, see Eq. (19). For the studied coronal region, our results indicate that the left-hand resonant instability develops for strongly oblique wave propagation with respect to the ambient magnetic field, with a maximum growth rate

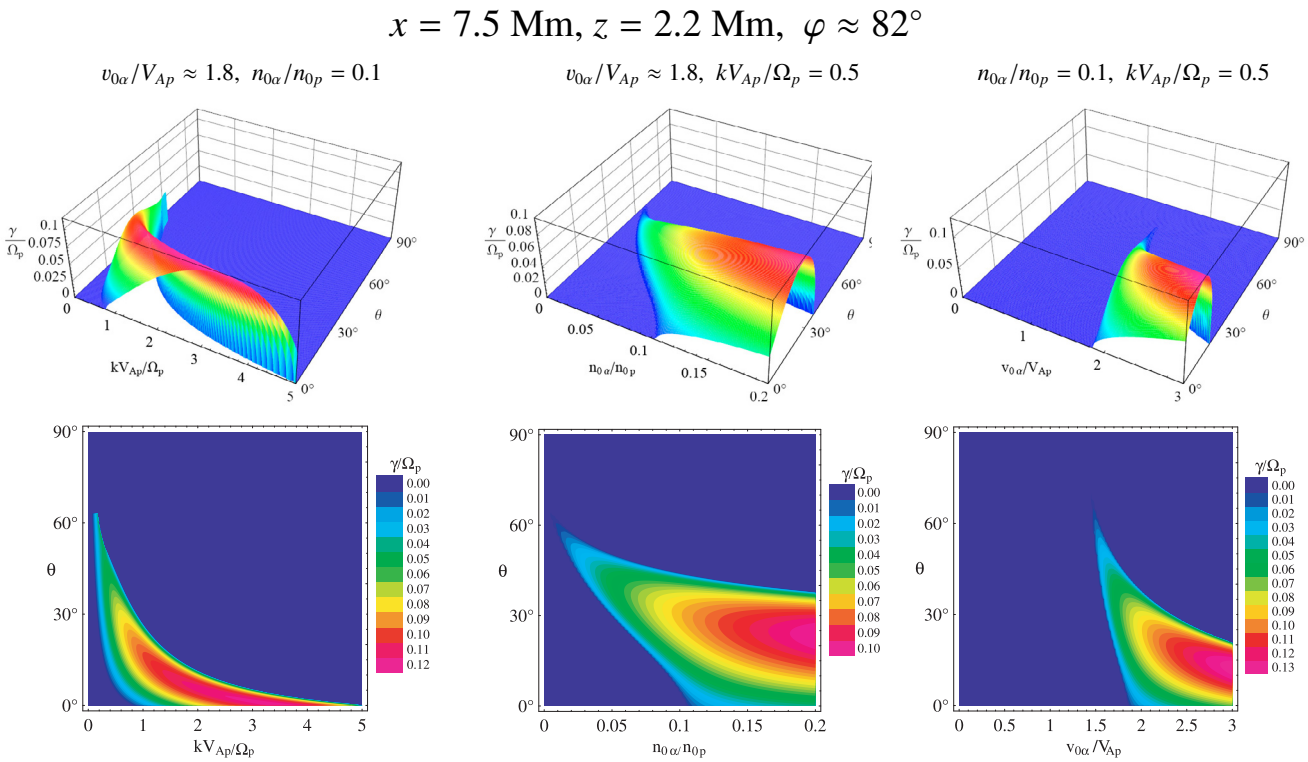

Fig. 4. Growth rate of the left-hand resonant ion-cyclotron instability, in the case of an alpha particle beam plasma. *Left*: as a function of the angle of propagation θ and the normalized wave number $kV_{\rm Ap}/\Omega_{\rm p}$ and for an alpha beam density $n_{0\alpha} = 0.1n_{0\rm p}$ and velocity $v_{0\alpha} = 320\ {\rm km\,s^{-1}} = 1.8V_{\rm Ap}$. *Middle*: as a function of θ and $n_{0\alpha}$ and for $v_{0\alpha} = 320\ {\rm km\,s^{-1}} \approx 1.8V_{\rm Ap}$ and $kV_{\rm Ap}/\Omega_{\rm p} = 0.5$. *Right*: as a function of θ and $v_{0\alpha}/v_{\rm Ap}$ and for $n_{0\alpha} = 0.1n_{0\rm p}$ and $kV_{\rm Ap}/\Omega_{\rm p} = 0.5$. Here $T_{0\rm e} = T_{0\rm p} = T_{0\alpha}$.

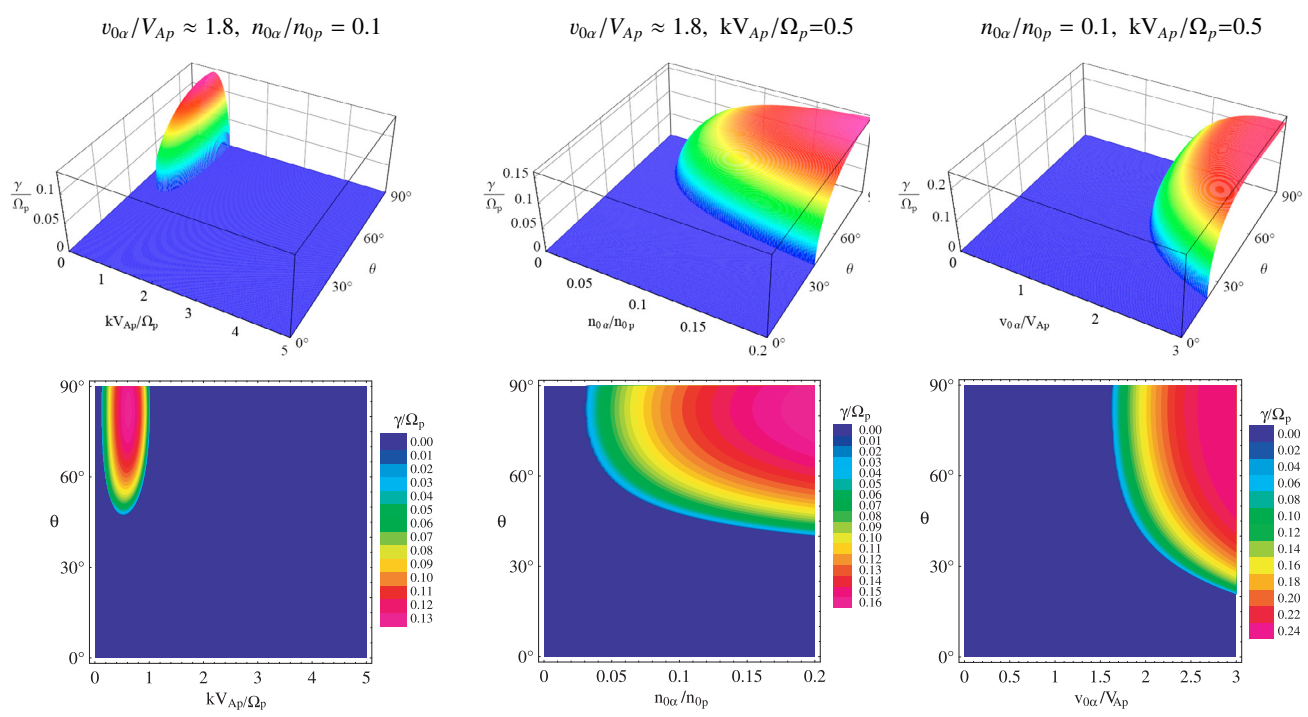

Fig. 5. Growth rate of the right-hand resonant ion-cyclotron instability, in the case of an alpha particle beam plasma. *Left*: as a function of the angle of propagation θ and the normalized wave number $kV_{\rm Ap}/\Omega_{\rm p}$ and for an alpha beam density $n_{0\alpha} = 0.1n_{0\rm p}$ and velocity $v_{0\alpha} = 320\ {\rm km\,s^{-1}} = 1.8V_{\rm Ap}$. *Middle*: as a function of θ and $n_{0\alpha}$ and for $v_{0\alpha} = 320\ {\rm km\,s^{-1}} \approx 1.8V_{\rm Ap}$ and $kV_{\rm Ap}/\Omega_{\rm p} = 0.5$. *Right*: as a function of θ and $v_{0\rm b}/v_{\rm Ap}$ and for $n_{0\alpha} = 0.1n_{0\rm p}$ and $kV_{\rm Ap}/\Omega_{\rm p} = 0.5$. Here $T_{0\rm e} = T_{0\rm p} = T_{0\alpha}$.

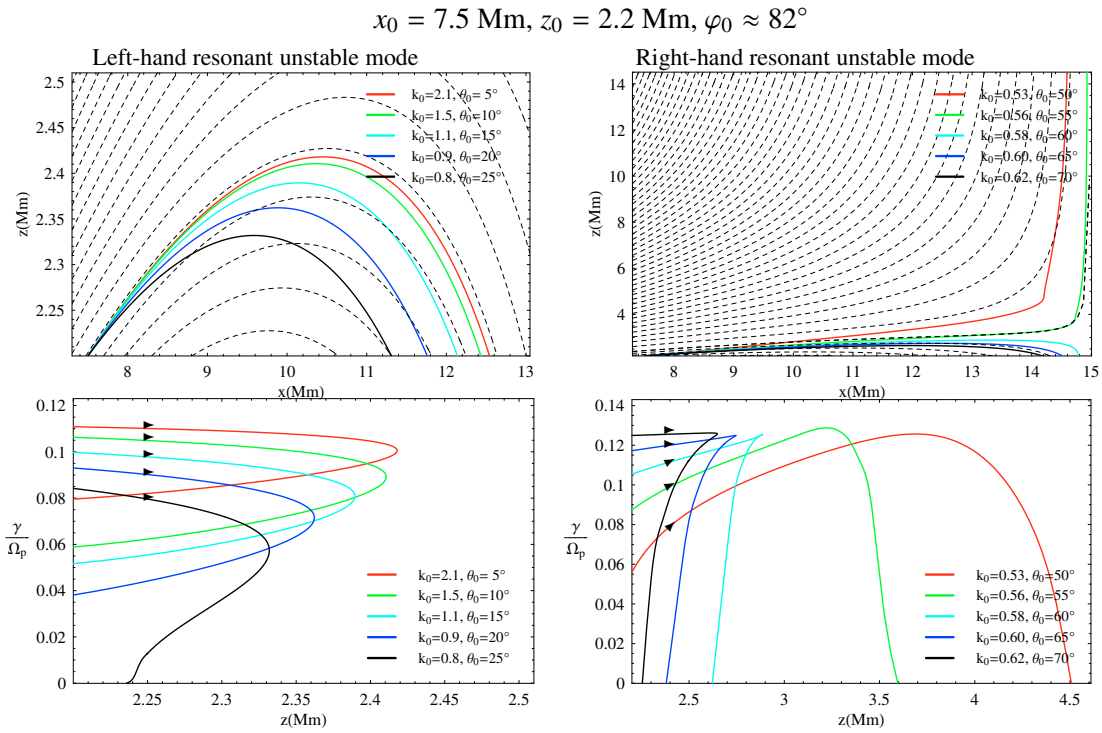

Fig. 6. The ray trajectory (*top*) and growth rate (*bottom*) of the left-hand (*left*) and the right-hand (*right*) resonant ion-cyclotron instabilities in the coronal funnel. These unstable modes are launched at the initial location (x_0 = 7.5 Mm and z_0 = 2.2 Mm) in the funnel (with a $\boldsymbol{B}_0$-inclination angle $\varphi_0 \approx 82°$), for different initial angle of propagation θ_0 and wave number k_0 chosen at the maximum instability growth rate. The dashed lines represent the magnetic field lines in the funnel.

at a quasi-perpendicular propagation, and disappears for weakly oblique propagation. In contrast, the right-hand instability develops for a weakly-oblique propagation to the ambient magnetic field, with a maximum growth rate at quasi-parallel propagation, and ceases for highly oblique or quasi-perpendicular propagation.

The non-local ray-tracing analysis revealed that both instabilities are sensitively affected by the magnetic field geometry and found to propagate closely along the field lines. The left-hand resonant instability is rapidly reflected, thus obeying the constraints imposed by a closed-field configuration. The associated growth rate slightly decreases and eventually cancels along the ray path. On the other hand, the right-handed resonant instabilities are also very well guided along the magnetic field lines of the funnel. This instability, for small initial angles of propagation, appears to follow the open field lines and can propagate higher up in the funnel, yet with a rapidly decreasing growth rate.

Consequently, fast ion beams in the magnetically open corona can provide enough energy for driving micro-instabilities through resonant wave-particle interactions. These instabilities may constitute in turn an important energy source for high-frequency ion-cyclotron waves which have been invoked to play a relevant role in the heating of coronal ions through cyclotron damping.

References

Axford, W. I., & McKenzie, J. F. 1992, in Solar Wind Seven Colloquium, ed. E. Marsch, & R. Schwenn, 1

Bernstein, I. B., & Friedland, L. 1984, in Basic Plasma Physics: Handbook of Plasma Physics, ed. A. A. Galeev, & R. N. Sudan, 1, 367

Boyd, T. J. M., & Sanderson, J. J. 1969, Plasma dynamics (London: Nelson)

Brekke, P., Kjeldseth-Moe, O., Brynildsen, N., et al. 1997, Sol. Phys., 170, 163

Cap, F. F. 1978, Handbook on plasma instabilities (New York: Academic Press), 2, 572

Cranmer, S. R., Field, G. B., & Kohl, J. L. 1999, ApJ, 518, 937

Feldman, W. C., Barraclough, B. L., Phillips, J. L., & Wang, Y.-M. 1996, A&A, 316, 355

Fontenla, J. M., Avrett, E. H., & Loeser, R. 1993, ApJ, 406, 319

Gabriel, A. H. 1976, Royal Society of London Philosophical Transactions Series A, 281, 339

Gary, S. P. 1993, Theory of Space Plasma Microinstabilities (UK: Cambridge University Press)

Hackenberg, P., Marsch, E., & Mann, G. 2000, A&A, 360, 1139

Hollweg, J. V. 2000, J. Geophys. Res., 105, 15699

Hollweg, J. V., & Isenberg, P. A. 2002, J. Geophys. Res. (Space Phys.), 107, 12

Innes, D. E., Inhester, B., Axford, W. I., & Willhelm, K. 1997, Nature, 386, 811

Isenberg, P. A., Lee, M. A., & Hollweg, J. V. 2000, Sol. Phys., 193, 247

Kohl, J. L., Noci, G., Antonucci, E., et al. 1997, Sol. Phys., 175, 613

Li, X., Habbal, S. R., Hollweg, J. V., & Esser, R. 1999, J. Geophys. Res., 104, 2521

Markovskii, S. A. 2001, ApJ, 557, 337

Markovskii, S. A., & Hollweg, J. V. 2004, Nonlinear Proc. Geophys., 11, 485

Marsch, E., & Tu, C.-Y. 2001, J. Geophys. Res., 106, 227

Mecheri, R., & Marsch, E. 2006, Royal Soc. London Philos. Trans. Ser. A, 364, 537

Ofman, L., Gary, S. P., & Viñas, A. 2002, J. Geophys. Res. (Space Phys.), 107, 9

Schrijver, C. J., Title, A. M., Harvey, K. L., et al. 1998, Nature, 394, 152

Stix, T. H. 1992, Waves in Plasmas (New York: American Institute of Physics)

Tu, C.-Y., Marsch, E., & Qin, Z.-R. 2004, J. Geophys. Res. (Space Phys.), 109, 5101

Vocks, C., & Marsch, E. 2001, Geophys. Res. Lett., 28, 1917

Voitenko, Y., & Goossens, M. 2002, Sol. Phys., 206, 285

Weinberg, S. 1962, Phys. Rev., 126, 1899

Xie, H., Ofman, L., & Viñas, A. 2004, J. Geophys. Res. (Space Phys.), 109, 8103